Large nonsaturating magnetoresistance and pressure-induced phase transition in the layered semimetal $HfTe_2$

S. Mangelsen,[1] P. G. Naumov,[2] O. I. Barkalov,[2,3] S. A. Medvedev,[2] W. Schnelle,[2] M. Bobnar,[2] S. Mankovsky,[4] S. Polesya,[4] C. Näther,[1] H. Ebert,[4] and W. Bensch[1,*]

[1]*Institute of Inorganic Chemistry, Christian-Albrechts University, Max-Eyth-Straße 2, 24118 Kiel, Germany*

[2]*Max Planck Institute for Chemical Physics of Solids, Nöthnitzer Straße 40, 01187 Dresden, Germany*

[3]*Institute of Solid State Physics, Russian Academy of Sciences, Academician Ossipyan Street 2, Chernogolovka, Moscow District, 142432, Russia*

[4]*Department of Chemistry, Physical Chemistry, Ludwig-Maximilians University, Butenandstrasse 5-13, 81377 Munich, Germany*

(Received 24 August 2017; revised manuscript received 23 October 2017; published 28 November 2017)

Unusual physical properties like large magnetoresistance (MR) and superconductivity occurring in semimetals with Dirac or Weyl points are often linked to their topologically nontrivial band structures. However, there is an increasing number of reports on semimetals that show large MR in the absence of Dirac or Weyl points. Herein we report an experimental and theoretical study on the layered transition-metal dichalcogenide (TMDC) $HfTe_2$ that shows a large MR of 1350% at $T = 2$ K and $\mu_0 H = 9$ T in the absence of Dirac or Weyl points. Moreover, the structure and electrical resistivity under pressure reveal a unique structural transition. These results clearly distinguish $HfTe_2$ from TMDCs like $MoTe_2$ or WTe_2 which both exhibit larger MR and are viewed as Weyl semimetals. $HfTe_2$ is an appealing platform for future investigations on the interplay of particular band-structure features and their connection to emerging physical properties.

DOI: 10.1103/PhysRevB.96.205148

I. INTRODUCTION

For a few years bulk semimetals have been in the focus of solid-state research, because of a plethora of observed unusual physical properties like large and nonsaturating magnetoresistance (MR), superconductivity, and their special topological properties. These compounds have been shown to be particularly interesting and suitable platforms to study the interplay between different crystal structures, chemical compositions, and resulting physical properties. While most of these materials have been known for a long time [1,2], recent progress in theoretical and experimental physics enabled the prediction and confirmation of Dirac semimetals like, e.g., Cd_3As_2 [3], Weyl semimetals like Nb and Ta monophosphide and arsenide [4], and (Mo,W)Te_2 [5–8]. The unusual properties of these compounds are of interest for both fundamental research and promising future applications, e.g., for spintronics devices.

In semimetals both electrons and holes contribute to the electrical conductivity caused by valence and conduction bands that cross the Fermi level. This can be realized at different points in momentum space, with the structures of, e.g., Bi or WTe_2 serving as prominent examples. Electronic bands touching at the same point in momentum space are realized in Heusler alloys and some silver chalcogenides with quadratic band dispersion or with linear dispersion in Dirac and Weyl semimetals [9]. Virtually all of these compounds are characterized by large or even extremely large and nonsaturating magnetoresistance effects at low temperatures; however, there is no universal approach to explain these effects. Classically, perfect compensation of electron and hole carriers in semimetals will lead to a large transverse MR with a quadratic field dependence [10]. We note that there are also reports about the large MR materials $MoTe_2$ and WTe_2 leading to contradictory results concerning the degree of carrier compensation, but a strong temperature dependence of the Fermi surface was observed in these studies [11–17]. For Cd_3As_2 [3] and WTe_2 [18] the large MR was proposed to occur due to a topological protection of the carriers from backscattering in zero field. Recent work on, e.g., LaSb [19,20] and YSb [21–24] demonstrated that topologically trivial compounds can also display large nonsaturating MR effects and a hypothesis based on the classical picture combined with a strong mixing of p and d orbitals in the presence of strong spin-orbit coupling was developed [25].

Layered transition-metal dichalcogenides (TMDCs; TQ_2 with $T =$ e.g., Ti, Zr, Hf, Mo, W; $Q = S$, Se, Te) crystallize in a variety of structure types differing by the stacking sequence of the TQ_2 layers, the coordination environment of the transition-metal cations and structural distortions [1]. In the simplest structure type abbreviated as $1T$ the TQ_2 layers consisting of edge-sharing TQ_6 octahedra are stacked onto each other in the $\cdots$AAA$\cdots$ sequence. Between the individual layers a van der Waals gap is located. The $1T'$ [26] and T_d [27] polytypes can be derived from the $1T$ structure type by the introduction of distortions (see Fig. S1 in the Supplemental Material [28]). The $1T'$ and T_d structures are adopted by Mo and W ditellurides, both of which are candidates to be Weyl semimetals in the T_d polytype [6,7,29]. While the T_d polytype is the only structure reported for WTe_2, polytypism is observed for $MoTe_2$. The $2H$ polymorph is obtained at lower temperature and $1T'$ $MoTe_2$ can be quenched from high temperatures, depending on the stoichiometry [30]. The latter modification undergoes a transition to the T_d polytype upon cooling below ~250 K [29]. Except for semiconducting $2H$ $MoTe_2$, the other ditellurides of Mo and W are semimetals with coexisting electron and hole pockets at the Fermi surface [6,7,29,31]. Mo as well as W ditelluride exhibits a strong MR [29,31]; the T_d form of $MoTe_2$ is a superconductor ($T_c = 0.10$ K) at ambient pressure [29] while superconductivity can be achieved for WTe_2 only beyond 10.5 GPa [32].

*wbensch@ac.uni-kiel.de

$HfTe_2$ crystallizes in the 1*T* structure and is much less studied compared to other transition-metal ditellurides, likely due to its sensitivity to air and moisture. Until now only some fundamental properties were investigated like the structure and stoichiometry [33–35], the electric transport properties [33,36], the pressure dependence of electric transport and unit cell parameters [36,37], the thermopower [38], and the theoretical electronic band structure [39,40]. The experimental band structure was recently studied by angle-resolved photoemission spectroscopy (ARPES) on thin films [40], but several physical properties of $HfTe_2$ have not been investigated and data on, e.g., the high-pressure behavior are partially contradictory.

Here we report on the preparation, ambient-pressure magnetotransport, and specific heat, as well as high-pressure structural and electrical resistivity investigations of $HfTe_2$. The experiments are complemented by extensive *ab initio* calculations of the electronic structure at zero and 6.5 GPa nominal pressure in order to provide an understanding of the observed phenomena.

II. EXPERIMENTAL AND COMPUTATIONAL DETAILS

A. Synthesis

$HfTe_2$ has been prepared by heating weighed quantities of Hf (Strem, 99.6% excluding 2.2% Zr) and Te (Chempur, 99.999%, low oxygen) for 7 d in evacuated ($<1 \times 10^{-4}$ mbar) carbon-coated silica ampoules. The coating was obtained by pyrolysis of acetone and is required to suppress the attack of silica by Hf. Single crystals were synthesized by chemical vapor transport from powdered $HfTe_2$. Samples 1 and 2 were obtained with NH_4I (Riedel de Haën, >99.5%) as transport agent in a temperature gradient 750 °C → 900 °C and 650 °C → 750 °C, sample 3 with CBr_4 (Fluka, min. 98%) in a gradient ∼500 °C → 600 °C. Powders deteriorate within a few minutes upon exposure to air; single crystals change in color in about 2 h from shiny golden to black. Therefore all samples were handled and stored in an argon-filled glove box [$p(O_2) < 1$ ppm, $p(H_2O) < 1$ ppm].

B. Characterization

The stoichiometry of crystals from each batch was checked by energy dispersive x-ray spectroscopy (EDXS) (Zeiss Gemini Ultra Plus equipped with an Oxford Instruments X-act EDS detector); the ratio of Hf:Te was found to be 1:2. The powder for high-pressure experiments and ground single crystals of batches B1 and B2 were checked by powder x-ray diffraction (XRD) (Supplemental Material, Fig. S2 [28]) on a STOE STADI-P equipped with Cu $K\alpha_1$ radiation ($\lambda = 1.540\,598$ Å), a Ge(111) monochromator, and a DECTRIS MYTHEN 1K detector. Pawley fits were carried out using TOPAS-ACADEMIC [41]; the extracted cell parameters are given in the Supplemental Material, Table S1 [28].

Single crystals from batch 3 were mounted in inert oil and intensity data were measured using a STOE Image Plate Diffraction System (IPDS-2) with Mo $K\alpha$ radiation ($\lambda = 0.710\,73$ Å). A numerical absorption correction was performed using X-RED and X-SHAPE of the program package X-AREA [42]. The structure was refined against F^2 with SHELXL-2014 [43] using anisotropic displacement parameters for all atoms. Selected structural data and details of the structure determination can be found in the Supplemental Material, Table S2 [28].

C. Physical properties

Measurements of the electrical resistivity have been performed using a four-point method (Pt wires 25 µm, Ag epoxy) using low-frequency alternating current (PPMS, Quantum Design). Temperatures down to 0.10 K were realized with a home-built adiabatic demagnetization stage. The heat capacity was measured with a relaxation method (HC option, PPMS).

D. High-pressure experiments

For pressure generation, a diamond anvil cell (DAC) equipped with diamond anvils with 500-µm culets was used. The pressure was determined using the shift of the fluorescence line of ruby. All sample loading procedures were performed in an Ar glove box with an O_2 and H_2O content below 0.5 ppm. For electrical resistivity measurements a single crystal of suitable size was placed into the central hole of a tungsten gasket with an insulating cubic BN/epoxy layer. The electrical resistivity at different pressures in the temperature range 1.7–300 K was measured with a direct-current van der Pauw technique with Pt electrodes attached to the sample.

For synchrotron XRD studies, a powdered sample of $HfTe_2$ was loaded in the central hole (∼150-μm diameter) of a tungsten gasket preindented to ∼40 μm thickness with silicone oil as the pressure transmitting medium. The angle-dispersive XRD measurements were carried out at the ID-27 beamline at the European Synchrotron Radiation Facility (ESRF, Grenoble, France). The wavelength of the x rays (0.3738 Å) was selected using a Si(111) monochromator. The sample to image plate detector (MAR345) distance was refined using the diffraction data of Si. The two-dimensional powder images were integrated using the program FIT2D yielding intensity versus 2θ plots.

E. DFT calculations

The electronic structure properties have been investigated within the framework of density functional theory (DFT) using the general gradient approximation (GGA) with the parametrization for the exchange and correlation potential as given by Perdew, Burke, and Ernzerhof (PBE) [44].

The Vienna *Ab Initio* Simulation Package (VASP) [45,46] has been used for the optimization of the unit cell parameters a and c, and of the z coordinate of Te of $HfTe_2$ for the whole pressure region under consideration. The optimization has been performed accounting for the van der Waals corrections treated via the semiempirical DFT-D3 Grimme's method [47]. A k mesh with $21 \times 21 \times 21$ grid points and a kinetic energy cutoff at 440 eV were used for this computational step. The presented electronic structure has been calculated using the full-potential linearized augmented plane wave (LAPW) method as implemented in the ELK code [48]. A k sampling with $16 \times 16 \times 8$ k-points mesh within the Brillouin zone was used for these calculations. The plane-wave basis set was defined by the cutoff $K_{max} = 7/R_{MT}$, with R_{MT} being the average muffin-tin radius. The cutoff $l_{max} = 8$ for the angular momentum expansion of the wave functions was used inside the MT spheres. The calculations for the electronic transport

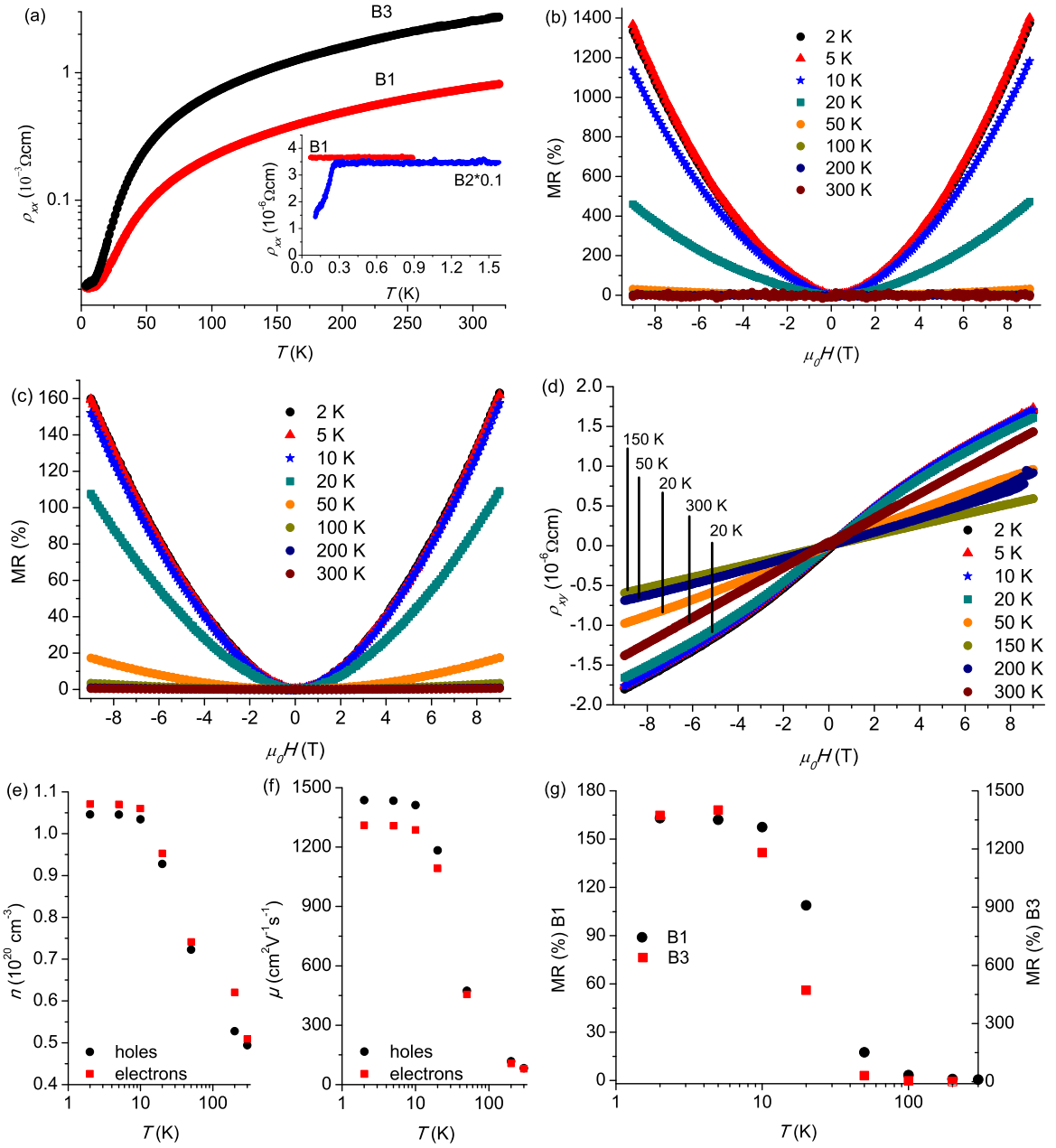

FIG. 1. Ambient-pressure magnetotransport properties of $HfTe_2$: (a) the temperature dependence of $\rho_{xx}(H = 0, T)$ for different samples; the inset shows the resistivity of B1 and B2 down to 0.1 K. (b) Field dependence of the transverse magnetoresistance (MR), $\rho_{xx}(H,T)$, for $HfTe_2$ (crystal B3) for selected temperatures. Magnetoresistance (c) and Hall-effect (d) data for sample S1. Carrier density (e) and mobility (f) extracted from Hall measurements on sample B1. (g) Temperature dependence of the MR for samples B1 and B3.

properties, based on the Kubo-Greenwood formalism, have been performed using the KKR Green's function method [49,50]. The temperature-dependent behavior of electrical resistivity has been calculated using the alloy analogy model that accounts for thermal lattice vibrations [51].

III. RESULTS AND DISCUSSION

A. Ambient pressure

Samples from differently prepared batches (B1, B2, B3) were investigated in this study (for details see Sec. II, Experimental and Computational Details). Structure analysis by x-ray diffraction (XRD) on a single crystal (B3) confirmed the symmorphic space group $P\text{-}3m1$ (for details see the Supplemental Material, Table S2 [28]). No significant residual electron density was found in the van der Waals gap that would point to a pronounced self-intercalation with excess Hf. The in-plane electrical resistivity, $\rho_{xx}(T)$, of $HfTe_2$ (B3) measured in the crystallographic ab plane is 2.7 mΩ cm at 300 K and decreases continuously with decreasing temperature [Fig. 1(a)] without displaying anomalies. The residual resistivity ratio (RRR) ranges from 36 (sample B1, grown at 900 °C) to 120 (B3, grown at 600 °C), surpassing even the value reported

in [38]. Resistivity measurements down to 0.10 K have been performed for samples B1 and B2, where only the one with the higher residual resistivity ρ_0 (B2) displays a gradual drop of $\rho(T)$ below 0.26 K, reaching about 40% of ρ_0 at 0.10 K [inset Fig. 1(a)]. This observation suggests the presence of a superconducting phase in this particular sample, as $HfTe_2$ is normal metallic down to $T = 0.10$ K. Possibly, superconductivity may be realized in crystals with increased RRR as reported for $MoTe_2$, where T_c increases with RRR [52].

The specific heat capacity, $C_p(T,H)$, of $HfTe_2$ (B1) measured in the temperature range 2–300 K (Supplemental Material, Fig. S3 [28] together with data from the literature for $MoTe_2$ [53,54] and WTe_2 [55]) exhibits no anomalies hinting to a phase transition. At low temperatures (Supplemental Material, inset of Fig. S3 [28]) $C_p(T,H)$ does not significantly depend on the magnetic field and is well described by $C_p(T) = \gamma T + \beta T^3 + \delta T^5$, where γT is the contribution due to conduction electrons and the remaining terms are lattice contributions. A fit of the data in the range 2.0−4.5 K results in $\gamma = 1.75(3)\,\mathrm{mJ\,mol^{-1}\,K^{-2}}$ and β corresponding to an initial Debye temperature $\theta_D(0) = 176$ K. The metal-like electrical conduction is in agreement with the small Sommerfeld coefficient γ and the calculated band structure (see Sec. III C).

Measurement of magnetotransport properties yields valuable insight into the characteristics of the charge carriers in the material. The transverse geometry with the current in the crystallographic ab plane and the magnetic field $\mu_0 H$ along c was applied to determine the MR $\rho_{xx}(H)$ and the Hall resistivity $\rho_{xy}(H)$. For $HfTe_2$ (B3) a positive MR is observed reaching 1350% at $T = 2$ K and $\mu_0 H = 9$ T [Fig. 1(b)] that shows no sign of saturation. For $T < 50$ K the field dependence of $\rho_{xx}(H)$ breaks the $(\mu_0 H)^2$ scaling that is expected in theory for perfectly compensated semimetals [10], and therefore the Kohler plots deviate from linearity (Supplemental Material, Fig. S4 [28]). The MR rapidly decreases with increasing temperature attaining only 5% at 100 K and 9 T, a common feature of the large MR of semimetals.

For sample B1 the MR is only 160% at $T = 2$ K and $\mu_0 H = 9$ T [Fig. 1(c)] which can be correlated with its lower RRR of 36, but still there is no sign of saturation. Similar observations were reported for other semimetals [3,56] where the carrier mobility and thus the MR increases with increasing RRR. Since RRR is usually an indication for the crystal purity and quality, it has to be noted that the hafnium used for the present study was of 97.4% purity (2.2% Zr, 0.4% other metals), which is among the highest available purity but still lower than the typically available purities that easily exceed 99.9% (e.g., in studies of WTe_2 [31,56]). The low purity level is due to the difficulties in the separation of Zr and Hf. A variation of the maximum MR over three orders of magnitude has been observed for WTe_2 depending on crystal quality and thus on the RRR value [56]; therefore a direct comparison of materials is difficult. The maximum reported values for the MR are 1.75×10^6% for WTe_2 [56] and 7.5×10^4% for $MoTe_2$ [15] ($T = 2$ K and $\mu_0 H = 9$ T). Under the same conditions, for $PdTe_2$ (isostructural to $HfTe_2$) prepared from high-purity elements a rather low maximum MR of ∼150% was reported [57]. Hence, it can be concluded that besides the actual electronic band structure, the purity of the materials and the crystal quality determine the MR value. For our best $HfTe_2$ crystal no Shubnikov–de Haas quantum oscillations were visible.

Hall resistivity measurements, $\rho_{xy}(H,T)$, conducted on sample B1 reveal by the sign of $\rho_{xy}(H,T)$ holes as the dominant charge carriers in the entire temperature range from 2 to 300 K [Fig. 1(d)]. We note that the isothermal field sweeps deviate from linearity for $T \leqslant 20$ K, indicating contributions from two carrier types with different concentrations [Fig. 1(d)]. Simultaneous fitting of MR (ρ_{xx}) and Hall-effect (ρ_{xy}) data within the two-band model yield at $T = 2$ K a maximum hole mobility $\mu_h = 1440\,\mathrm{cm^2\,V^{-1}\,s^{-1}}$ and a similar electron mobility μ_e of $1310\,\mathrm{cm^2\,V^{-1}\,s^{-1}}$ [Fig. 1(f)]. These values are lower than those reported for $MoTe_2$ or WTe_2 (up to 10^4−$10^5\,\mathrm{cm^2\,V^{-1}\,s^{-1}}$) [15,56], presumably caused by the factors affecting the MR as discussed above. The carrier concentrations are estimated to be of the order of $1 \times 10^{20}\,\mathrm{cm^{-3}}$ [Fig. 1(e)] with only slight deviations from compensation ($n_h/n_e \approx 0.97$). Both mobility and carrier densities decrease with increasing temperature by similar increments, pointing to a remarkably good compensation of the carrier types within the applied model. The remarkable resemblance of $\mu(T)$, $n(T)$, and MR(T) [Fig. 1(g)] suggests an interconnection of these parameters, which is reasonable within the theory of orbital MR [10]. The decay of the MR with increasing temperature is presumably linked to the decreasing carrier mobility [58]. However, the fits applied here can only be seen as an estimate as they do not perfectly match the data for $T \leqslant 50$ K. Therefore, the description within the framework of the two-band model is not fully satisfying for the observed transport properties, while contributions from carriers of further carrier pockets are supported by our DFT calculations (*vide infra*).

B. High pressure

The behavior of layered TMDCs under high pressure has attracted considerable attention since they are systems exhibiting strongly competing effects of charge-density wave (CDW) formation and superconductivity [59]. One of the recent prominent examples is $TiSe_2$ [60]. Contrary to $TiSe_2$, no CDW formation is observed in $HfTe_2$ as is clearly seen from the resistivity and Hall-effect measurements as well as from a structure examination [36], while no superconductivity in $HfTe_2$ is observed at ambient pressure. Data on the high-pressure behavior of $HfTe_2$ are so far scarce and contradictory [36,37]. Therefore, we have studied the electrical conductivity and structural behavior of $HfTe_2$ for pressures up to 45 GPa.

The pressure evolution of the electrical resistivity, $\rho_{xx}(T,p)$, of $HfTe_2$ is shown in Fig. 2. At the lowest applied pressure of 1.1 GPa the resistivity shows a typical metal-like behavior, in agreement with ambient-pressure data. The room-temperature resistivity $\rho(300\,\mathrm{K})$ decreases smoothly with p up to ∼5 GPa and starts to rise again at higher pressures (inset in Fig. 2), in agreement with published data [36]. A sluggish structural phase transition to a weakly metallic (or even semiconducting) phase was proposed to explain the observed rise of $\rho(300\,\mathrm{K})$ at high pressure [36]. Our powder XRD data (Fig. 3) indicate, however, that the CdI_2-type structure of $HfTe_2$ at ambient pressure remains stable to at least $p \sim 12$ GPa. Thus the increase of $\rho(300\,\mathrm{K})$ at $p \geqslant 5$ GPa is due to changes of the electronic structure of $HfTe_2$.

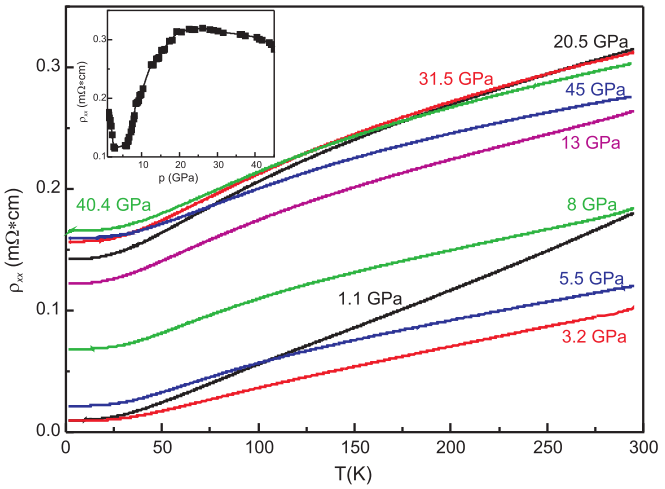

FIG. 2. Temperature dependence of electrical resistivity of $HfTe_2$ at selected pressures. The inset shows the nonmonotonic dependence of the room-temperature resistivity on pressure.

Increasing the pressure above 12 GPa, the appearence of additional reflections in the XRD patterns (Fig. 3) indicates the onset of a structural phase transition. The transition is indeed very sluggish and two phases coexist over a large pressure range, followed by a single-phase pattern at $p \approx 27$ GPa. The quality of the XRD patterns is poor due to pressure-induced line broadening, preferred-orientation effects, and the strong background due to Compton electron scattering in the stressed diamond anvils. These effects prevent a full structure determination of the high-pressure (HP) phase.

Nevertheless, the diffraction pattern collected at 27 GPa can be indexed with an orthorhombic lattice with parameters $a = 4.37(4)$ Å, $b = 5.16(6)$ Å, and $c = 2.66(4)$ Å (Fig. 3). It

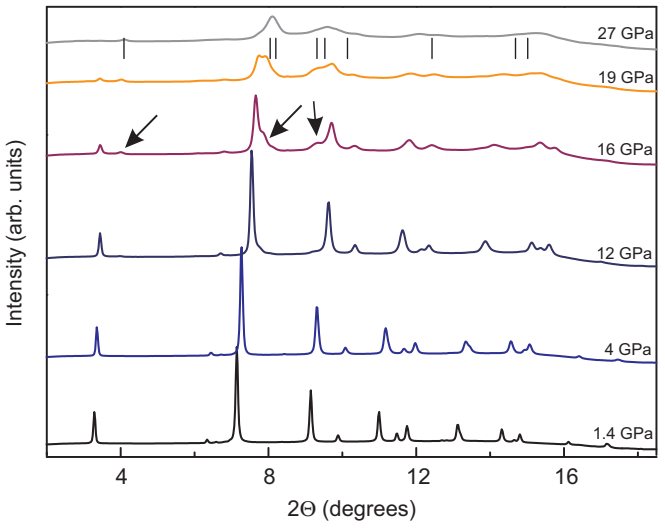

FIG. 3. Powder x-ray diffraction patterns of $HfTe_2$ at different pressures. The ambient-pressure CdI_2-type structure remains stable up to pressures above 12 GPa. The appearence of additional diffraction peaks (arrows) indicates the onset of a structural phase transition. Ticks below the pattern at 27 GPa mark the calculated reflection positions of the orthorhombic lattice.

can be supposed that the HP phase of $HfTe_2$ adopts a marcasite-type structure. Such a structure seems likely in $HfTe_2$ since the marcasite structure is intermediate between the CdI_2- and the densest pyrite-type structure [1] and a pressure-induced phase transition from CdI_2 to pyrite structure was observed in $IrTe_2$ [61]. It has to be noted that the pyrite HP structure of $IrTe_2$ was obtained only with laser heating of the sample, which implies a large energetic separation of the HP phase. This may be the reason for the broad two-phase region observed for $HfTe_2$ in our experiments.

The temperature dependence of $\rho(T)$ at all pressures up to 45 GPa is clearly metal-like; thus the HP phase of $HfTe_2$ is metallic (or a strongly doped semimetal). However, the transition to the proposed marcasite-type structure is associated with a changeover of the dimensionality: While CdI_2 is a layered structure with quasi-two-dimensional properties the marcasite type exhibits typical three-dimensional behavior. Thus the observed nonmonotonic pressure behavior of the resistivity reflects changes of the electronic band structure due to the dimensionality crossover. No superconductivity has been observed in either phase of $HfTe_2$ up to 45 GPa during cooling down to 1.7 K.

C. DFT calculations

In order to gain further insight into the origin of the observed transport phenomena the electronic band structure of $HfTe_2$ has been calculated for the ground state and for $p = 6.5$ GPa. The ground-state band structure is presented in Fig. 4(a) and allows us to classify $HfTe_2$ as a semimetal with two hole pockets around Γ and two electron pockets located around M and L [see also the Fermi surface plot in Fig. 4(c)]. Therefore, holes and electrons are well separated in k space. The calculated density of states (DOS) of 0.96 states eV^{-1} f.u.$^{-1}$ [f.u.: formula unit; see Fig. 5(a) for details] is in line with the experimental result (0.74 states eV^{-1} f.u.$^{-1}$) estimated from our measurement of the heat capacity. The occurrence of Weyl points can be ruled out from the inversion symmetry present in space group $P\text{-}3m1$, and moreover no Dirac points are visible at or near the Fermi energy. The electron pockets have a pronounced Hf-d character whereas there is a strong mixing of Hf-d and Te-p based bands comprising the hole pockets, especially on the inner pocket. Obviously, in semimetal systems, charge neutrality requires parity of the numbers of holes and electrons in the pockets created by the bands crossing E_F. However, the electric transport is governed by the holelike and electronlike carriers present at E_F, and their numbers can be different. In any case, the occurrence of a large MR suggests that this carrier compensation is reasonably good in $HfTe_2$ and the mixed orbital character of the pockets [25] provides an additional approach for an explanation. We note that deviations from the recently reported calculated band structure [40] (i.e., the overlap of two bands slightly above E_F at Γ) are likely due to the Te positions which are different from those used in [40]. For the present calculations relaxed positions were used (see Supplemental Material, Table S3 [28]) that deviate from the ideal value $z = 0.25$ and are perfectly in line with our experimental results and former reports [34]. If $z = 0.25$ is used in our calculations we are able to reproduce the band

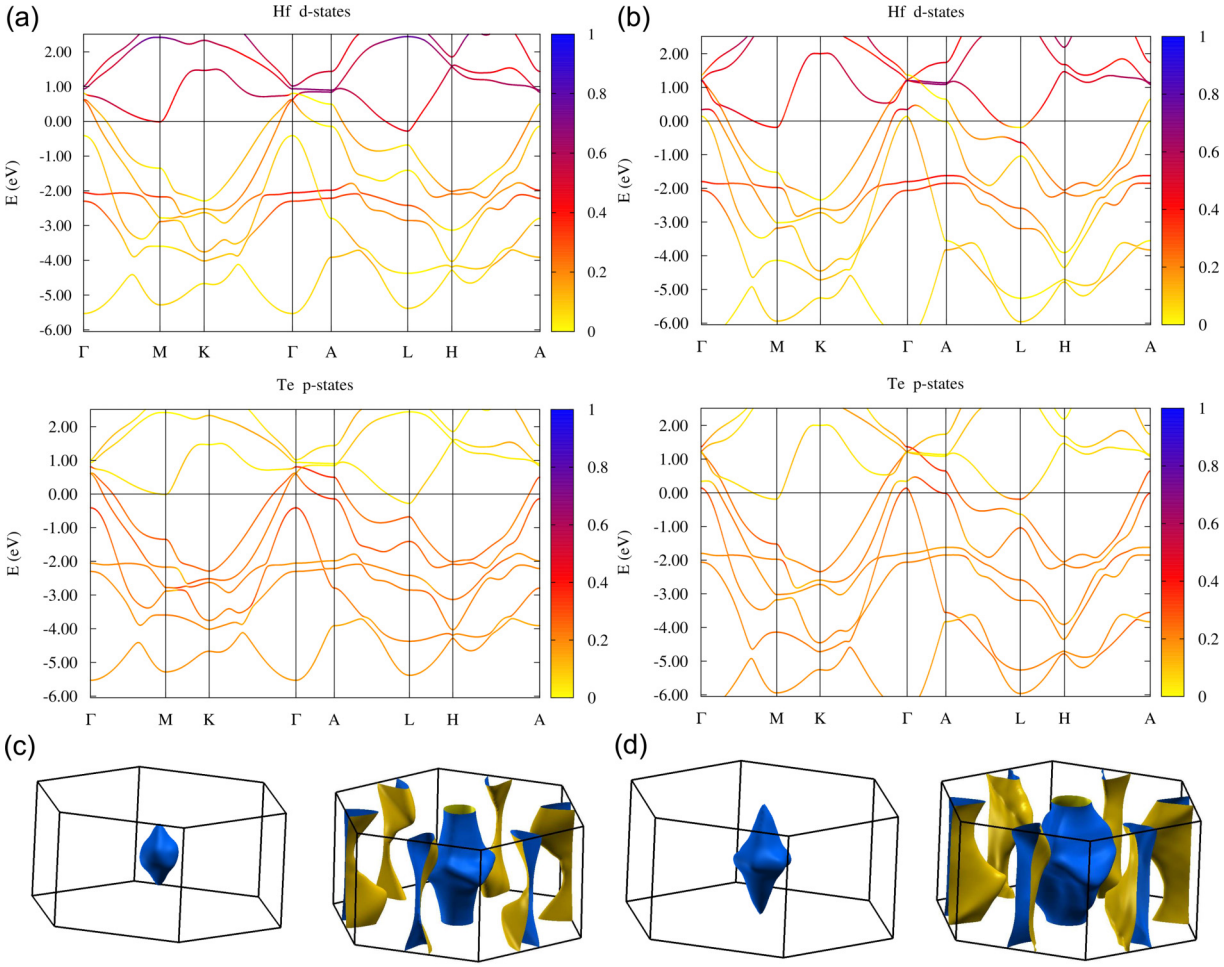

FIG. 4. Calculated electronic structure of $HfTe_2$: the calculated band structures for ambient pressure (a) and $p = 6.5$ GPa (b) are presented and resolved according to the contributions coming from Hf d and Te p states. Other orbitals are neglected due to their low contributions. In (c,d) plots of the Fermi surface are shown for the respective pressures. The Fermi surface for the innermost energy band at the Γ point is shown separately. The additional Fermi surface for the small pocket at the Γ point appearing for $p = 6.5$ GPa is not presented.

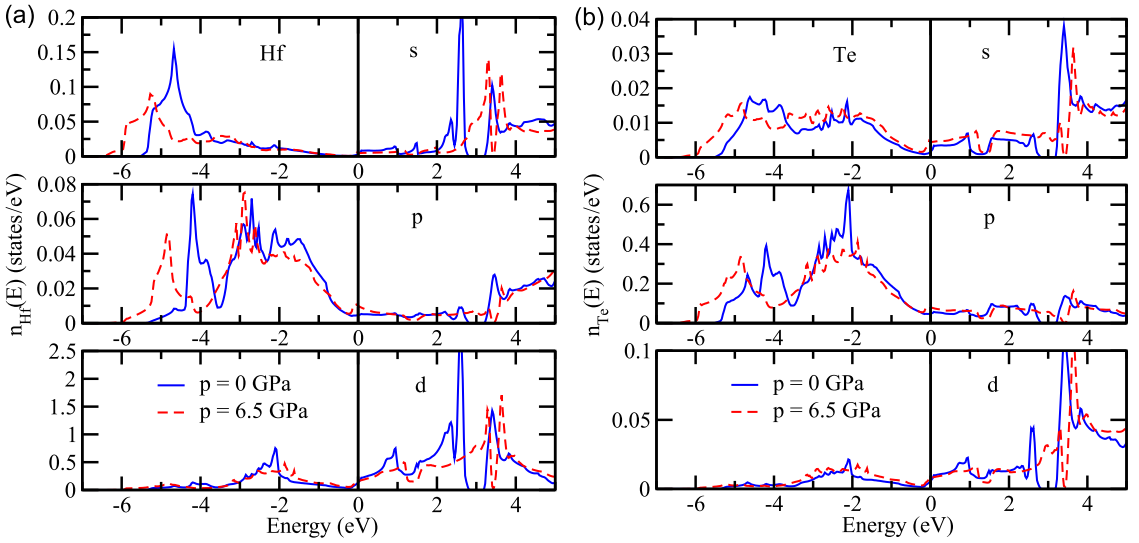

FIG. 5. Density of states (DOS) for Hf (a) and Te (b) sites for $HfTe_2$ in the ground state (solid blue line) and under the pressure of 6.5 GPa (dashed red line).

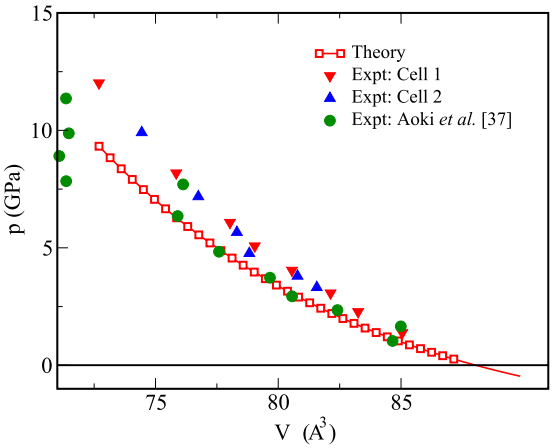

FIG. 6. Calculated pressure dependence of the volume for $HfTe_2$ in comparison with experimental results [37].

structure reported [40] with good agreement. The change in orbital texture from Te-p to Hf-d could not be confirmed, and it should be emphasized that there is a strong mixing instead of a clear orbital character.

The pressure-induced changes of the electronic band structure of $HfTe_2$ have been calculated by optimization of the structural parameters and of the atomic coordinates by minimizing the total energy of the system for each volume decrease with increasing pressure. The calculated volume evolution with increasing pressure accounting for structure relaxation is presented in Fig. 6 and is compared to available experimental data. The optimized structure parameters for the ground state and for $p = 6.5$ GPa are listed in the Supplemental Material, Table S3 [28].

The electronic band structure and Fermi surfaces at $p = 6.5$ GPa are plotted in Figs. 4(b) and 4(d), respectively. The pressure increase leads to a broadening of the energy bands (see also DOS in Fig. 5) and the modification of the electronic states around the Fermi level induces an increase of the area of the Fermi surface [Fig. 4(d)]. However, this change does not result in significant alterations of the DOS at E_F, which increases from 0.96 states eV^{-1} f.u.$^{-1}$ at $p = 0$ GPa to 1.22 states eV^{-1} f.u.$^{-1}$ at $p = 6.5$ GPa. On the other hand, the observed structural phase transition under pressure can be associated with a change of the Fermi surface topology occurring at the pressure when the Fermi surfaces corresponding to different energy bands touch each other. Moreover, pressure leads to changes of both the band dispersion and their orbital character. An additional hole pocket is created along the Γ-A direction by a Te-p band crossing the Fermi level and band inversion occurs along the L-A direction giving rise to an even stronger mixing of orbital character for that electron pocket. The calculated temperature-dependent resistivity at ambient pressure agrees rather well with our experimental results. Moreover the initially declining and then increasing resistivity at room temperature is partly reproduced by our calculations (Fig. 7), however, with deviations especially at lower temperatures.

$HfTe_2$ displays a strong MR effect much larger than in common metals, and the magnitude is most likely limited by impurities. The origin of the MR can be ascribed to carrier compensation and the mixed orbital character of the hole pockets. However, the simple picture of just one type of hole and electron compensation cannot be supported from the calculated band structure as multiple hole and electron pockets are predicted. This multiband picture is also likely to account for the formerly reported complex temperature dependence of the Seebeck coefficient [38]. On the other hand, this could also point to temperature-induced changes of the Fermi surface, as recently proposed for WTe_2 [14] and $MoTe_2$ [16]. Thus the actual band structure of $HfTe_2$ is of great interest and therefore future ARPES studies on bulk $HfTe_2$ would be valuable to confirm the actual electronic structure and yield further insight into the origin of the large MR effect.

In the ongoing discussion on the origin of large MR effects our results build a bridge between the TMDCs $MoTe_2$ and WTe_2 as Weyl semimetals and the increasing number of examples within the family of the La and Y pnictides that show remarkable MR effects without this feature. Among the layered TMDCs $HfTe_2$ is unified with $MoTe_2$ and WTe_2 by the occurrence of a large MR; however, the actual crystallographic and band structure differ. Very appealing from the view of fundamental research is that the absence of Weyl points in

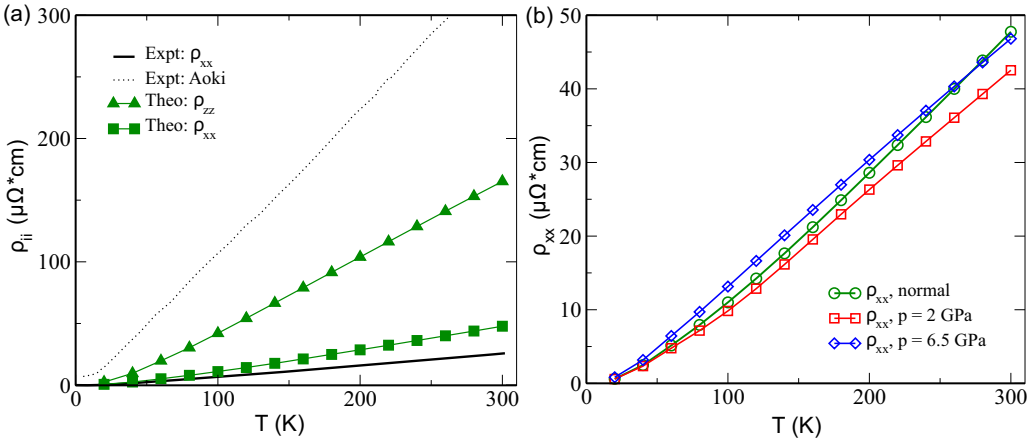

FIG. 7. (a) Resistivities for ρ_{xx} (squares) and for ρ_{zz} (triangles) calculated for $HfTe_2$ in comparison with the experimental results for ρ_{xx} (solid line). The dotted line represents the experimental data obtained by Aoki *et al.* [37]; (b) resistivity data calculated for different pressures.

$HfTe_2$ is not accompanied by absence of the MR; thus this compound provides an alternative platform to study this effect separated from the Weyl topology.

The experimental and theoretical results on $HfTe_2$ under pressure pave the way for future studies of this material with pressure as a useful parameter to influence the Fermi surface and the resulting electric transport properties in a reasonably large pressure window. The yet unknown HP phase of $HfTe_2$ motivates future studies of its structure and properties.

IV. CONCLUSIONS

In conclusion, we present a study of the magnetotransport properties of $HfTe_2$ and a structural transition under pressure. The mechanism behind the large and unsaturated MR effect of up to 1350% appears to be linked to its semimetallic nature with coexisting electrons and holes on the Fermi surface and the additional strong orbital mixing of Te *p* and Hf *d* states, especially for the hole pockets as revealed by our DFT calculations. Thus $HfTe_2$ provides an alternative platform to study the origin of large MR in semimetals and layered TMDCs in the absence of topological features like Dirac or Weyl points. This holds great potential to further understand the emergence of large MR effects and their connection to these topological features.

ACKNOWLEDGMENTS

Financial support by the Deutsche Forschungsgemeinschaft Grant No. ME 3652/3-1 as well as the State of Schleswig-Holstein is gratefully acknowledged. We acknowledge the European Synchrotron Radiation Facility (ESRF) for granting beam time at ID27 and Dr. M. Mezouar and Dr. G. Garbarino (ESRF) for assistance in using the beamline. Christin Szillus is acknowledged for help with the EDX measurements.

[1] J. A. Wilson and A. D. Yoffe, Adv. Phys. **18**, 193 (1969).
[2] F. Hulliger, in *Structure and Bonding*, edited by C. K. Jørgensen, J. B. Neilands, Sir Ronald S. Nyholm, D. Reinen, and R. J. P. Williams (Springer, Berlin, Heidelberg, 1968), pp. 83–229.
[3] T. Liang, Q. Gibson, M. N. Ali, M. Liu, R. J. Cava, and N. P. Ong, Nat. Mater. **14**, 280 (2014).
[4] Z. K. Liu, L. X. Yang, Y. Sun, T. Zhang, H. Peng, H. F. Yang, C. Chen, Y. Zhang, Y. F. Guo, D. Prabhakaran, M. Schmidt, Z. Hussain, S.-K. Mo, C. Felser, B. Yan, and Y. L. Chen, Nat. Mater. **15**, 27 (2016).
[5] I. Belopolski, S.-Y. Xu, Y. Ishida, X. Pan, P. Yu, D. S. Sanchez, H. Zheng, M. Neupane, N. Alidoust, G. Chang, T.-R. Chang, Y. Wu, G. Bian, S.-M. Huang, C.-C. Lee, D. Mou, L. Huang, Y. Song, B. Wang, G. Wang *et al.*, Phys. Rev. B **94**, 085127 (2016).
[6] Y. Sun, S.-C. Wu, M. N. Ali, C. Felser, and B. Yan, Phys. Rev. B **92**, 161107 (2015).
[7] A. A. Soluyanov, D. Gresch, Z. Wang, Q. Wu, M. Troyer, X. Dai, and B. A. Bernevig, Nature **527**, 495 (2015).
[8] K. Deng, G. Wan, P. Deng, K. Zhang, S. Ding, E. Wang, M. Yan, H. Huang, H. Zhang, Z. Xu, J. Denlinger, A. Fedorov, H. Yang, W. Duan, H. Yao, Y. Wu, S. Fan, H. Zhang, X. Chen, and S. Zhou, Nat. Phys. **12**, 1105 (2016).
[9] C. Shekhar, A. K. Nayak, Y. Sun, M. Schmidt, M. Nicklas, I. Leermakers, U. Zeitler, Y. Skourski, J. Wosnitza, Z. Liu, Y. Chen, W. Schnelle, H. Borrmann, Y. Grin, C. Felser, and B. Yan, Nat. Phys. **11**, 645 (2015).
[10] A. B. Pippard, *Magnetoresistance in Metals*, 1st ed. (Cambridge University Press, Cambridge, 2009).
[11] C.-L. Wang, Y. Zhang, J.-W. Huang, G.-D. Liu, A.-J. Liang, Y.-X. Zhang, B. Shen, J. Liu, C. Hu, Y. Ding, D.-F. Liu, Y. Hu, S.-L. He, L. Zhao, L. Yu, J. Hu, J. Wei, Z.-Q. Mao, Y.-G. Shi, X.-W. Jia *et al.*, Chin. Phys. Lett. **34**, 097305 (2017).
[12] I. Pletikosić, M. N. Ali, A. V. Fedorov, R. J. Cava, and T. Valla, Phys. Rev. Lett. **113**, 216601 (2014).
[13] S. Thirupathaiah, R. Jha, B. Pal, J. S. Matias, P. K. Das, P. K. Sivakumar, I. Vobornik, N. C. Plumb, M. Shi, R. A. Ribeiro, and D. D. Sarma, Phys. Rev. B **95**, 241105 (2017).
[14] Y. Wu, N. H. Jo, M. Ochi, L. Huang, D. Mou, S. L. Bud'ko, P. C. Canfield, N. Trivedi, R. Arita, and A. Kaminski, Phys. Rev. Lett. **115**, 166602 (2015).
[15] Q. Zhou, D. Rhodes, Q. R. Zhang, S. Tang, R. Schönemann, and L. Balicas, Phys. Rev. B **94**, 121101 (2016).
[16] F. C. Chen, H. Y. Lv, X. Luo, W. J. Lu, Q. L. Pei, G. T. Lin, Y. Y. Han, X. B. Zhu, W. H. Song, and Y. P. Sun, Phys. Rev. B **94**, 235154 (2016).
[17] T. Zandt, H. Dwelk, C. Janowitz, and R. Manzke, J. Alloys Compd. **442**, 216 (2007).
[18] J. Jiang, F. Tang, X. C. Pan, H. M. Liu, X. H. Niu, Y. X. Wang, D. F. Xu, H. F. Yang, B. P. Xie, F. Q. Song, P. Dudin, T. K. Kim, M. Hoesch, P. K. Das, I. Vobornik, X. G. Wan, and D. L. Feng, Phys. Rev. Lett. **115**, 166601 (2015).
[19] F. F. Tafti, Q. D. Gibson, S. K. Kushwaha, N. Haldolaarachchige, and R. J. Cava, Nat. Phys. **12**, 272 (2015).
[20] L.-K. Zeng, R. Lou, D.-S. Wu, Q. N. Xu, P.-J. Guo, L.-Y. Kong, Y.-G. Zhong, J.-Z. Ma, B.-B. Fu, P. Richard, P. Wang, G. T. Liu, L. Lu, Y.-B. Huang, C. Fang, S.-S. Sun, Q. Wang, L. Wang, Y.-G. Shi, H. M. Weng *et al.*, Phys. Rev. Lett. **117**, 127204 (2016).
[21] O. Pavlosiuk, P. Swatek, and P. Wiśniewski, Sci. Rep. **6**, 38691 (2016).
[22] N. J. Ghimire, A. S. Botana, D. Phelan, H. Zheng, and J. F. Mitchell, J. Phys.: Condens. Matter **28**, 235601 (2016).
[23] J. He, C. Zhang, N. J. Ghimire, T. Liang, C. Jia, J. Jiang, S. Tang, S. Chen, Y. He, S.-K. Mo, C. C. Hwang, M. Hashimoto, D. H. Lu, B. Moritz, T. P. Devereaux, Y. L. Chen, J. F. Mitchell, and Z.-X. Shen, Phys. Rev. Lett. **117**, 267201 (2016).
[24] J. Xu, N. J. Ghimire, J. S. Jiang, Z. L. Xiao, A. S. Botana, Y. L. Wang, Y. Hao, J. E. Pearson, and W. K. Kwok, Phys. Rev. B **96**, 075159 (2017).
[25] F. F. Tafti, Q. Gibson, S. Kushwaha, J. W. Krizan, N. Haldolaarachchige, and R. J. Cava, Proc. Natl. Acad. Sci. USA **113**, E3475 (2016).
[26] B. E. Brown, Acta Crystallogr. **20**, 268 (1966).
[27] A. Mar, S. Jobic, and J. A. Ibers, J. Am. Chem. Soc. **114**, 8963 (1992).

[28] See Supplemental Material at http://link.aps.org/supplemental/10.1103/PhysRevB.96.205148 for additional data on the structure, heat capacity, and Kohler plots.
[29] Y. Qi, P. G. Naumov, M. N. Ali, C. R. Rajamathi, W. Schnelle, O. Barkalov, M. Hanfland, S.-C. Wu, C. Shekhar, Y. Sun, V. Süß, M. Schmidt, U. Schwarz, E. Pippel, P. Werner, R. Hillebrand, T. Förster, E. Kampert, S. Parkin, R. J. Cava *et al.*, Nat. Commun. **7**, 11038 (2016).
[30] D. H. Keum, S. Cho, J. H. Kim, D.-H. Choe, H.-J. Sung, M. Kan, H. Kang, J.-Y. Hwang, S. W. Kim, H. Yang, K. J. Chang, and Y. H. Lee, Nat. Phys. **11**, 482 (2015).
[31] M. N. Ali, J. Xiong, S. Flynn, J. Tao, Q. D. Gibson, L. M. Schoop, T. Liang, N. Haldolaarachchige, M. Hirschberger, N. P. Ong, and R. J. Cava, Nature **514**, 205 (2014).
[32] D. Kang, Y. Zhou, W. Yi, C. Yang, J. Guo, Y. Shi, S. Zhang, Z. Wang, C. Zhang, S. Jiang, A. Li, K. Yang, Q. Wu, G. Zhang, L. Sun, and Z. Zhao, Nat. Commun. **6**, 7804 (2015).
[33] D. Hodul and M. J. Sienko, Physica B+C (Amsterdam) **99**, 215 (1980).
[34] J. G. Smeggil and S. Bartram, J. Solid State Chem. **5**, 391 (1972).
[35] L. Brattås, A. Kjekshus, S. E. Rasmussen, S. Svensson, J. Koskikallio, and S. Kachi, Acta Chem. Scand. **25**, 2783 (1971).
[36] P. C. Klipstein, D. R. P. Guy, E. A. Marseglia, J. I. Meakin, R. H. Friend, and A. D. Yoffe, J. Phys. C: Solid State Phys. **19**, 4953 (1986).
[37] Y. Aoki, T. Sambongi, H. Takahashi, N. Mori, F. Levy, and H. Berger, Synth. Met. **71**, 1883 (1995).
[38] Y. Aoki, T. Sambongi, F. Levy, and H. Berger, J. Phys. Soc. Jpn. **65**, 2590 (1996).
[39] A. Hussain Reshak and S. Auluck, Phys. B **363**, 25 (2005).
[40] S. Aminalragia-Giamini, J. Marquez-Velasco, P. Tsipas, D. Tsoutsou, G. Renaud, and A. Dimoulas, 2D Mater. **4**, 015001 (2017).
[41] A. A. Coelho, TOPAS-ACADEMIC, Version 4.1 (Coelho Software, Brisbane, Australia, 2007).
[42] X-AREA (STOE & CIE GmbH, Darmstadt, Germany, 2008).
[43] G. M. Sheldrick, Acta Crystallogr., Sect. C: Struct. Chem. **71**, 3 (2015).
[44] J. P. Perdew, K. Burke, and M. Ernzerhof, Phys. Rev. Lett. **77**, 3865 (1996).
[45] G. Kresse and J. Furthmüller, Phys. Rev. B **54**, 11169 (1996).
[46] G. Kresse and J. Furthmüller, Comput. Mater. Sci. **6**, 15 (1996).
[47] S. Grimme, J. Antony, S. Ehrlich, and H. Krieg, J. Chem. Phys. **132**, 154104 (2010).
[48] ELK code, http://elk.sourceforge.net/.
[49] H. Ebert *et al.*, *The Munich SPR-KKR Package*, Version 7.7 (Munich, 2012), http://olymp.cup.uni-muenchen.de/ak/ebert/SPRKKR.
[50] H. Ebert, D. Ködderitzsch, and J. Minár, Rep. Prog. Phys. **74**, 096501 (2011).
[51] H. Ebert, S. Mankovsky, K. Chadova, S. Polesya, J. Minár, and D. Ködderitzsch, Phys. Rev. B **91**, 165132 (2015).
[52] D. Rhodes, R. Schönemann, N. Aryal, Q. Zhou, Q. R. Zhang, E. Kampert, Y.-C. Chiu, Y. Lai, Y. Shimura, G. T. McCandless, J. Y. Chan, D. W. Paley, J. Lee, A. D. Finke, J. P. C. Ruff, S. Das, E. Manousakis, and L. Balicas, Phys. Rev. B **96**, 165134 (2017).
[53] F. C. Chen, X. Luo, R. C. Xiao, W. J. Lu, B. Zhang, H. X. Yang, J. Q. Li, Q. L. Pei, D. F. Shao, R. R. Zhang, L. S. Ling, C. Y. Xi, W. H. Song, and Y. P. Sun, Appl. Phys. Lett. **108**, 162601 (2016).
[54] R. Sankar, G. Narsinga Rao, I. P. Muthuselvam, C. Butler, N. Kumar, G. Senthil Murugan, C. Shekhar, T.-R. Chang, C.-Y. Wen, C.-W. Chen, W.-L. Lee, M.-T. Lin, H.-T. Jeng, C. Felser, and F. C. Chou, Chem. Mater. **29**, 699 (2017).
[55] J. E. Callanan, G. A. Hope, R. D. Weir, and E. F. J. Westrum, J. Chem. Thermodyn. **24**, 627 (1992).
[56] M. N. Ali, L. Schoop, J. Xiong, S. Flynn, Q. Gibson, M. Hirschberger, N. P. Ong, and R. J. Cava, EPL Europhys. Lett. **110**, 67002 (2015).
[57] Y. Wang, J. Zhang, W. Zhu, Y. Zou, C. Xi, L. Ma, T. Han, J. Yang, J. Wang, J. Xu, L. Zhang, L. Pi, C. Zhang, and Y. Zhang, Sci. Rep. **6**, 31554 (2016).
[58] P.-J. Guo, H.-C. Yang, B.-J. Zhang, K. Liu, and Z.-Y. Lu, Phys. Rev. B **93**, 235142 (2016).
[59] R. A. Klemm, Phys. C **514**, 86 (2015).
[60] A. F. Kusmartseva, B. Sipos, H. Berger, L. Forró, and E. Tutiš, Phys. Rev. Lett. **103**, 236401 (2009).
[61] J. M. Léger, A. S. Pereira, J. Haines, S. Jobic, and R. Brec, J. Phys. Chem. Solids **61**, 27 (2000).